RESEARCH ARTICLE

Multi-Channel, Actively Shielded, Power Efficient MRI Z-Gradient Cylindrical Coil Design Using Target-Field Method

HAILE BAYE KASSAHUN, **SADEQ S ALSHARAFI**, (Member, IEEE),
AHMED M BADAWI, (Senior Member, IEEE),
AND ABDEL-MONEM M EL-SHARKAWY, (Member, IEEE)
Systems and Biomedical Engineering, Faculty of Engineering, Cairo University, Giza, Egypt

Corresponding author: Haile Baye Kassahun (haile.kassahun.a@eng-st.cu.edu.eg)

ABSTRACT Gradient coils are essential for MRI where fast and large electrical current pulses are typically applied to conventional, single-channel gradient coils, particularly for high-performance gradient applications. However, these pulses result in significant power losses and heating of the coil. We investigate the design of power-efficient multi-channel Z-gradient coils operating in the conventional mode comparing them to conventional single-channel coils designed using similar dimensions and alike DC performance characteristics. The power-efficiencies of thirteen different two-channel configurations having various section lengths for two different dimensions are analyzed. The current density of each section is approximated by Fourier series expansion where a linear equation relating the desired target field and current density is formulated and then solved. A stream function is derived from the obtained current density and then used to extract the final winding patterns of each section using a particular track width and a specific number of turns. The design process involves optimizing the current driving each channel, the distribution of coil windings, and the section size. Similarly, the performance of three-channel coils is also investigated. Results show that a power dissipation reduction of 17-28% and ~23% can be achieved using two- and three-channel coils, respectively. Moreover, we showed that multi-channel coils may have a slightly better shielding efficiency compared to conventional coils. A new methodology for designing two- and three-channel coils is presented where an advantage in terms of power efficiency can be gained depending on design parameters, coil's dimensions, number of turns, and other metrics.

INDEX TERMS Gradient coil array, MRI, power dissipation, stream function, and target-field method.

I. INTRODUCTION

The gradient coils are critical components of Magnetic resonance imaging (MRI) scanner. They are responsible to generate linearly varying magnetic fields to localize (spatially encode) the MR signal. The gradient coils are constituted of three sets to generate magnetic fields in the X, Y, and Z directions within the imaging region, which is usually

The associate editor coordinating the review of this manuscript and approving it for publication was Marco Giannelli.

defined by a diameter of spherical volume (DSV). The majority of human MRI scanners have cylindrical gradient coils. Desirable characteristics of gradient coils include low power dissipation, high linearity, low inductance, minimal stray field, minimal interaction with the rest of the MRI system components…etc.

Various methods to design gradient coils of desirable characteristics were shown over the last three to four decades [1]. The discrete wire design and continuous current density methods are considered to be the two main

gradient design methods. In discrete wire-space methods, the general coil pattern is initially selected based on *a priori* knowledge or experience then optimization algorithms are used to optimize the position of the coils. This gradient coil design technique may be computationally intensive [2].

The continuous current density method is mainly based on the target-field method initially introduced by Turner [3]. The current density surface can be represented by stream functions where discretization is employed using numerical techniques such as finite difference method (FDM) [4], finite element method (FEM) [5], or boundary element method (BEM) [6], [7], [8], [9] to relate the stream-functions to the desired target via a set of linear equations. The current intensity and winding patterns are derived from the obtained stream function [10], [11]. The solution requires fine meshing and is computationally expensive. On the other hand, the current density on the coil's surface can be written as a Fourier series expansion [12], [13], [14], [15], [16], [17], [18], [19] where a set of linear equations relating the Fourier coefficients and the desired field at specific locations are formulated to solve an inverse problem. The parametric stream function is then computed where current intensities and winding patterns are obtained. This method is proved to be relatively computationally efficient albeit it is restricted to particular geometries. It is noted that regularization is needed for both of the later methods to achieve a stable solution for an ill-posed problem.

Recently, new multi-channel or matrix gradient coils were introduced [20], [21], [22], [23], [24], [25], [26], [27], [28]. Matrix gradient coils are usually designed by properly arranging multiple similar coil elements on cylindrical or biplanar surfaces. Unlike single-channel coil, each coil element in matrix gradient coil is driven by its own independent gradient amplifier. Matrix gradient coils are able to generate both linear and nonlinear spatially varying magnetic fields [22]. Even though these designs have great flexibility to produce different field patterns over the DSV, they require a large number of amplifiers for driving each coil element. Moreover, the total dissipated power used to drive a linear gradient field can be relatively higher than that of a conventional coil [26]. Taraghinia [28] designed a three-channel unshielded Z-gradient coil array system by driving each channel with an independent amplifier. They divided the cylindrical surface into equal sections and assigned an equal number of turns for each section to dynamically change the magnetic field. An advantage of using multi-channel coils is to reduce the power requirements of current amplifiers used despite the increase in their numbers. Also, a design based on an equal division of surfaces with an equal number of turns each does not necessarily provide optimal power efficiency for the linear gradient mode. Takrimi and Atalar [29], [30] modified further the previous Z-gradient coil array by adding an active shielding array. Recently, we showed that a two-channel unshielded bi-planar Z-gradient coil design operating in the conventional linear mode can achieve better power efficiency

compared to a single-channel design of similar dimensions and gradient field requirements [31].

In this paper, we focus on the design of multi-channel gradient coils exploring the DC power reduction advantage of two- and three-channel actively shielded Z-gradient coils compared to that of a single-channel one with similar dimensions and performance metrics. We also investigate how the changes in coil dimensions may affect such gains. The target-field method is used to compute current densities and wire patterns. For the two-channel coil, both the primary and secondary coils are divided into four sections where each channel consists of two symmetric sections with respect to Z = 0 plane each having similar current densities but in opposite directions. Current densities of coil sections associated with each channel are approximated by Fourier-series expansion. Linear equations relating the desired target field and the current densities are formulated and solved. A stream function is derived from the obtained current density and then used to extract the final winding patterns of each section using a particular track width and a specific number of turns. The size of each section of the primary and shielding coils was varied with a fixed incremental length in the longitudinal direction until an efficient design of optimal geometry is obtained. The two symmetrical primary and corresponding shielding sections are driven by the same current intensity. The DC-power was calculated for each solution and then the coil configuration with the least power was finally chosen.

Following similar procedures, another three-channel coil was designed. The three-channel had two independent channels for the primary coil and a third channel was associated with the shielding coil surface. The number of turns for all designs was optimized keeping the total number of turns equal. The dissipated power comparisons of all multi-channel and conventional coil configurations were performed at a fixed total number of turns on the primary coil surface.

As will be shown, the proposed multi-channel coil designs resulted in a gradient coil with higher power efficiency in comparison to a single-channel coil with similar characteristics and dimensions. Moreover, the multi-channel coils may have a slightly better shielding efficiency. It is noted that the reduction achieved in DC dissipated power for multi-channel gradient coils is dependent on the design parameters, coil's dimension, and number of turns for a specific coil dimension.

II. METHODS

Fig. 1 illustrates the proposed cylindrical gradient coil configuration. The configuration shows the division of the primary and shielding surfaces of a Z-gradient coil into four sections each along the length of the surface (Z direction). The primary coils are located on the inner cylindrical surface that has a radius R_a and length L_a. Similarly, the shielding coils are positioned on the surface of the middle cylinder with a radius R_b and length L_b. The first channel consists of the peripheral two symmetric sections of the primary coils (section one $(L_s$ to $L_a/2)$ and section four $(-L_a/2$ to $-L_s)$) as well as the peripheral two symmetric sections of the shielding coils
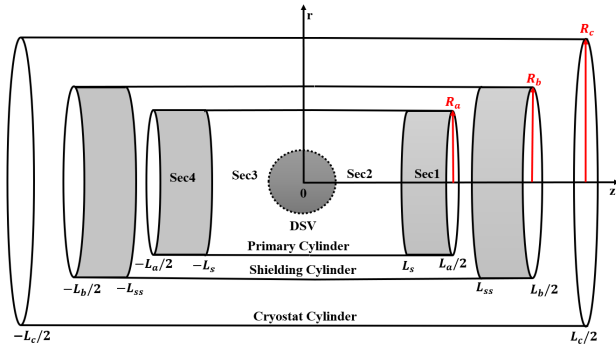
FIGURE 1. Schematic diagram showing the coordinate system of the primary and shielding two-channel coils. The first channel consists of the two annular pairs (shaded gray) on the primary and shielding coil surfaces, whereas the second channel consists of the rest of the sections. The outer cylinder is the cryostat and the inner spherical region is the DSV.

(section one (L_{ss} to $L_b/2$) and section four ($-L_b/2$ to $-L_{ss}$)). The second channel consists of the two middle symmetrical sections of the primary coils (section two (0 to L_s) and section three ($-L_s$ to 0)) as well as the two middle symmetrical sections of the shielding coils (section two (0 to L_{ss}) and section three ($-L_{ss}$ to 0)). The outer cylinder with a radius R_c and length L_c is the cryostat surface where 256 uniformly distributed points are sampled.

As shown in [4], the magnetic flux density, **B**, at any point on the DSV and the stray field regions can be generally calculated from the current density $\mathbf{J}(\mathbf{r}_i)$ as follows:

$$\mathbf{B}(\mathbf{r}_o) = \frac{\mu_0}{4\pi} \int_S \frac{\mathbf{J}(\mathbf{r}_i) \times \mathbf{R}}{R^3} \mathbf{dS} \quad (1)$$

where μ_0 is the permeability of free space, $\mathbf{J}(\mathbf{r}_i) = J_r \mathbf{e}_r + J_\theta \mathbf{e}_\theta + J_z \mathbf{e}_z$ is the current density expressed in cylindrical coordinates, $\mathbf{R} = \mathbf{r}_o - \mathbf{r}_i$ is the displacement vector from the source region ($\mathbf{r}_i (r, \theta, z)$) to the target region ($\mathbf{r}_o (x_o, y_o, z_o)$), and $\mathbf{dS}$ is the surface element integral. Expressing the current density in cartesian coordinates as $\mathbf{J} = (J_r \cos(\theta) - J_\theta \sin(\theta))\mathbf{a}_x + (J_r \sin(\theta) + J_\theta \cos(\theta))\mathbf{a}_y + (J_z)\mathbf{a}_z$ where no current flows in the radial direction, and $\mathbf{R} = (x_o - r \cos(\theta))\mathbf{a}_x + (y_o - r \sin(\theta))\mathbf{a}_y + (z_o - z)\mathbf{a}_z$, equation (1) is used to yield the longitudinal component of the magnetic flux density given by:

$$\mathbf{B}_z$$
$$= \frac{\mu_0}{4\pi} \int_{L_{init}}^{L_{term}} \int_0^{2\pi} \frac{J_\theta(r - y_o \sin(\theta) - x_o \cos(\theta))}{R^3} r d\theta dz \quad (2)$$

where

$$R = \sqrt{(x_o - r \cos(\theta))^2 + (y_o - r \sin(\theta))^2 + (z_o - z)^2},$$

the variables r, L_{init} and L_{term} are the radius, initial, and terminal longitudinal positions of the cylindrical surface, respectively.

In this study, the performances of various self-shielded designs by varying the lengths of the primary and corresponding shielding sections were investigated. For the primary coil, the length of the first section was varied from the smallest

length ($\frac{1}{10}L_a$) to ($\frac{4}{10}L_a$) with an incremental length ($\Delta L = \frac{1}{40}L_a$). The corresponding length of the second section can also be simultaneously obtained from the length of the first section as:

$$L_f = \frac{L_a}{10} + m \times \frac{L_a}{40}$$
$$L_s = \frac{L_a}{2} - L_f \quad (3)$$

where L_f and L_s are the lengths of the first and second sections, respectively, and $m = 0, 1, 2, 3, 4, 5, 6, 7, 8, 9, 10, 11, 12$. This results in 13 different two-channel Z-gradient coil configurations out of which the most power-efficient design was chosen. The length of each corresponding section for the shielding coil was also proportionally updated.

For each design configuration, the current density of each section was expanded using Fourier series approximation. The induced gradient field for the Z-gradient coil is anti-symmetric with respect to the Z-direction [12], [13], [14] and current flows only in the angular direction ($J_z = 0$). It has been previously shown that the current density of each independent section can be expanded using Fourier series expansion [19] where the current densities at each boundary vanish to zero. Accordingly, for the two-channel Z-gradient coils, the Fourier series expansion of section (i) is expressed as follows:

$$J_{\theta i}(z) = \sum_{n=1}^{N_i} a_{ni} \sin(\frac{n\pi(z - L_{init})}{L_{sec}}), \quad i = 1, 2, 3, 4 \quad (4)$$

where $J_{\theta i}$ is the angular component of the current density of ith section of primary coils. N_i is the number of finite terms of the Fourier series expansion for i^{th} section of primary coils. The variable a_{ni} is the unknown Fourier series coefficient of ith section. $L_{sec} = L_f$ for the first and fourth sections and $L_{sec} = L_s$ for the second and third sections. L_{init} is equal to L_s, 0, 0, and $-L_s$ for sections one, two, three, and four, respectively. The ranges of z are $L_s \leq z \leq L_a/2$, $0 \leq z \leq L_s$, $-L_s \leq z \leq 0$, and $-L_a/2 \leq z \leq -L_s$ for first, second, third, and fourth sections, respectively (see Fig. 1). A similar expression was derived for the Fourier series expansions of current densities of the corresponding shielding coils where the length and radius of the coils will now be L_b and R_b, respectively.

For the primary Z-gradient coils, the Z component magnetic flux density on the DSV can be obtained by substituting (4) into (2) and is given by:

$$B_z(x_o, y_o, z_o) = \sum_{i=1}^{4} \sum_{n=1}^{N_i} a_{ni} C_{ni} \quad (5)$$

where

$$C_{ni}$$
$$= \frac{\mu_0}{4\pi} \int_{L_{init}}^{L_{term}} \int_0^{2\pi} \frac{D_i(r - y_o \sin(\theta) - x_o \cos(\theta))}{R^3} R_a d\theta dz \quad (6)$$

where

$D_1 = \sin(\frac{n\pi(z-L_s)}{L_f})$, $D_2 = \sin(\frac{n\pi z}{L_s})$, $D_3 = \sin(\frac{n\pi z}{L_s})$, $D_4 = \sin(\frac{n\pi(z+L_s)}{L_f})$, R_a is the radius of the primary coil, and C_{ni} is the coefficient matrix (C_n) of ith section, $i = 1, 2, 3, 4$.

The Z component of the magnetic flux density on the stray field region can be similarly obtained from the current densities of primary and shielding cylindrical surfaces using the Biot-Savart law. We used a total of $M = 256$ points on the DSV and $Q = 256$ points on the cryostat to simultaneously calculate the magnetic flux densities of the two regions using the expression:

$$B_{zk} = \sum_{i=1}^{4} \sum_{n=1}^{N_{pi}} a_{ni}^p C_{k,ni}^p + \sum_{i=1}^{4} \sum_{n=1}^{N_{si}} a_{ni}^s C_{k,ni}^s \quad (7)$$

where $k = 1, 2, \ldots, M + Q, N_{pi}$ and N_{si} are the maximum number of Fourier series coefficients (NFSC) of the ith section of primary (p) and shielding (s) coils, respectively. A maximum number of NFSC $= 8$ for each section was used for the current density function approximation (other studies used 4-5 coefficients [16], [18]). The variables a_{ni}^p and a_{ni}^s are the unknown Fourier series coefficient of ith section of primary and shielding coils, respectively. The variables $C_{k,ni}^p$ and $C_{k,ni}^s$ are the coefficients of the primary and shielding coils which were determined by using (6) and computed by the built-in MATLAB® numerical integration function *integral2* (the Math Works®, Inc. MATLAB®). Given the target field points on the DSV and stray-field regions, the following linear equation can be formed from (7).

$$Ax = b \quad (8)$$

where x is a column vector of the unknown Fourier series coefficients $(a_{ni}^p, \ldots, a_{ni}^s)^T$, $b = (b_1, b_2, \cdots, b_{M+Q})^T$ is a column vector of the given target field (DSV and stray field regions), the matrix A with dimension $((M+Q) \times (8 \times \text{NFSC}))$ is the coefficient matrix derived from $C_{k,ni}^p$ and $C_{k,ni}^s$. Therefore, if we let $N = 8 \times \text{NFSC}$ and $U = M + Q$, then the equivalent matrix equation of (8) will be:

$$\begin{bmatrix} A_{11} & A_{12} & \cdots & A_{1N} \\ A_{21} & A_{22} & \cdots & A_{2N} \\ \vdots & \vdots & \vdots & \vdots \\ A_{U1} & A_{U2} & \cdots & A_{UN} \end{bmatrix} \begin{bmatrix} x_1 \\ x_2 \\ \vdots \\ x_N \end{bmatrix} = \begin{bmatrix} b_1 \\ b_2 \\ \vdots \\ b_U \end{bmatrix}. \quad (9)$$

Equation (9) is an ill-posed inverse problem, so regularization is needed to get a practically feasible solution. In this work, the well-known Tikhonov's regularization [32], [33], [34] was used and the unknown Fourier series coefficients were expressed as:

$$x_\lambda = argmin\{\|Ax - b\|_2^2 + \lambda^2 \|Lx\|_2^2\} \quad (10)$$

where $\lambda > 0$ is the regularization parameter and L is the regularization matrix. The value of λ was iteratively selected from the predetermined range $(5 \times 10^{-11}$ to $1.75 \times 10^{-8})$ around the corner value of the L-curve using the regularization tool [34] to minimize both the maximum field deviation on the DSV and maximum stray field on the cryostat [19]. The

final expression for the unknown Fourier series coefficients can be expressed by simplifying (10) as:

$$x_\lambda = (A^T A + \lambda^2 L^T L)^{-1} A^T b. \quad (11)$$

The matrix $(L^T L)$ was deduced from the penalty function given below. For the primary Z-gradient coils, the functions can be expressed as:

$$F_i = \int_{L_{init}}^{L_{term}} \int_0^{2\pi} \left(\frac{\partial J_{\theta i}}{\partial z}\right)^2 R_a d\theta dz, \quad i = 1, 2, 3, 4 \quad (12)$$

where F_i is the penalty function of each section of the primary coil and $J_{\theta i}$ is the angular component current density of each section (i). Similar expressions can be formulated for the shielding coils. Here, the penalty function is used to reduce the maximum current density variation and widen the wire spacing [4]. The current densities with the equivalent Fourier series expansions (4) can be substituted into (12) and the following expressions were obtained after simplification of the analytical integration (12).

$$L_{npi} = \frac{n^2 \pi^3 R_a}{L_{sec}}, \quad i = 1, 2, 3, 4 \quad (13)$$

where L_{npi} is the regularization vector for the ith section of primary coil, R_a is the radius of the primary coil, L_{sec} is the length of each section, and $n = 1, 2, \ldots, \text{NFSC}$.

$$L_{nsi} = \frac{n^2 \pi^3 R_b}{L_{secs}}, \quad i = 1, 2, 3, 4 \quad (14)$$

where L_{nsi} is the regularization vector for i^{th} section of shielding coil, R_b is the radius of the shielding coil and L_{secs} is the length of each section of the shielding coil.

The matrix $(L^T L)$ in (11) was obtained by concatenating all the eight vectors given above diagonally [18], [35]. An iterative method was then used to solve (11). As a result, using the change of variables, $A' = A^T A + \lambda^2 L^T L$ and $b' = A^T b$, the Krylov subspace iterative method namely GMRES (generalized minimal residual) method [36] was applied to solve (11). Once the Fourier series coefficient column vector (x_λ) is determined, the current densities of both primary and shielding coils can be calculated by using (4).

The winding patterns of the primary and shielding coils were obtained from the stream function. The stream function can be derived from the surface current density by using the current continuity equation [4] given by:

$$\nabla \cdot \mathbf{J} = 0 \quad (15)$$

where $\mathbf{J}$ can be expressed in terms of the stream function ψ [4] as:

$$\mathbf{J} = \nabla \times \psi \mathbf{e}_r$$
$$J_\theta = \frac{\partial \psi}{\partial z} \quad (16)$$

where ψ is the stream function. Therefore, for Z-gradient coils, the stream functions can be found by integrating the

angular component of the current densities (4). Accordingly, the stream functions of each section (*i*) are given by:

$$\psi_{pni} = -\sum_{n=1}^{N_{pi}} (a_{ni}^p) \frac{L_{sec}}{n\pi} \cos(\frac{n\pi (z - L_{init})}{L_{sec}}), \quad i = 1, 2, 3, 4 \tag{17}$$

where ψ_{pni} are the stream functions of ith section of the primary coil. The Fourier series coefficients were calculated by using (11). Similarly, the stream functions of the corresponding shielding sections were also calculated by using (17) where the lengths are now substituted by the shielding-section dimensions.

Once the stream functions are determined, the current for the primary and corresponding shielding sections can be calculated. First, for each configuration, the optimal number of turns of each section that satisfies <5% maximum field deviation on the DSV and <5 Gauss maximum stray field on the cryostat was determined. The details are illustrated in the flow chart diagram (see Fig. 2). If the optimal number of turns of the primary coils are N_{tp1}, N_{tp2}, N_{tp3}, and N_{tp4} for sections one, two, three, and four, respectively, then, the currents of each section can be calculated based on [10] as follows:

$$I_i = \frac{max(\psi_{pni}) - min(\psi_{pni})}{N_{tpi}}, \quad i = 1, 2, 3, 4 \tag{18}$$

where I_i, N_{tpi}, $max(\psi_{pni})$, and $min(\psi_{pni})$ are the current, the number of turns, maximum stream function value, and minimum stream function value of ith section of the primary coil, respectively.

Here, $N_{tp1} = N_{tp4}$, $N_{tp2} = N_{tp3}$, $I_1 = -I_4$, $I_2 = -I_3$ due to symmetry. For the two-channel coils (i.e., four-section primary and four-section shielding configurations), the current of ith section of the primary is the same as the current of ith section of the shielding coil ($i = 1, 2, 3, 4$). According to [10], once the currents are determined, the track locations are given by the contour lines whose stream function values are calculated by:

$$\psi'_{pni} = min(\psi_{pni}) + (j - 0.5)I_i, \quad i = 1, 2, 3, 4 \tag{19}$$

where ψ'_{pni} is the stream function values of the new contour lines of ith section, I_i is current of ith section, and $min(\psi_{pni})$ is the minimum stream function value of ith section, $j = 1, 2, \cdots, N_{tpi}$. The number of turns of the corresponding shielding sections can be obtained using the following equation:

$$N_{tsi} = round(N_{tpi} \frac{max(\psi_{sni}) - min(\psi_{sni})}{max(\psi_{pni}) - min(\psi_{pni})}), \quad i = 1, 2, 3, 4 \tag{20}$$

where N_{tsi}, $max(\psi_{sni})$, and $min(\psi_{sni})$ are the number of turns, maximum, and minimum stream functions of the shielding sections, respectively. An equation similar to (19) was used to calculate the locations of streamlines of the shielding surfaces. The detailed procedures for the optimization of section size and the number of turns per section are illustrated in the

flow chart diagram (Fig. 2). For the three-channel coils that have two channels on the primary cylinder and one independent channel associated with the secondary cylinder, all the aforementioned mathematical formulations and procedures were applied for the primary sections, whereas the shielding coil had a Fourier series expansion of current density given by:

$$J_\theta(z) = \sum_{n=1}^{N_s} a_{ns} \sin(\frac{2n\pi z}{L_b}), \quad -L_b \le z \le L_b \tag{21}$$

where J_θ is the current density, N_s is the number of Fourier series coefficients, a_{ns} are the unknown Fourier series coefficients, and L_b is the length of the shielding coil. Moreover, the shielding section had an equal number of turns as that of the conventional coil ($N_{ts} = 54$).

For each design passing the field deviation and stray field requirements, the minimum gap between consecutive contours and the total length of the contours of each section for both the two- and three-channel coils were calculated. The total resistance of each section (R_i) was then computed from the total length of extracted wires (winding patterns) and the cross-sectional area of the wires as:

$$R_i = \frac{\rho \times L_{Ti}}{A} \tag{22}$$

where ρ is the resistivity of copper, L_{Ti} is the total length of all contour wires of a section (digitizing resolution was less than 1.5 cm in both the Z and θ directions), and A is the cross-sectional area of the wire. The total dissipated DC power of each design was computed from the sum of powers of each section of primary and shielding coils. The total dissipated DC power of a certain configuration can be expressed as:

$$power = \sum_{i=1}^{N_{sec}} I_i^2 R_i \tag{23}$$

where I_i is the current of each section, R_i is the total resistance of each section, and N_{sec} is the total number of sections of a two- or three-channel configuration.

After the dissipated power and minimum wire spacing of all configurations passing the design criteria in Fig. 2 are obtained, the most power efficient configuration was selected. The total number of turns on the primary coil surface was fixed (NT = 78) for all configurations during the selection process. As a result, a configuration with the least dissipated power that satisfies minimum wire spacing above 5 mm and NT = 78 was chosen.

In this work, all scripts for all computations were developed in-house by using MATLAB® (the Math Works®, Inc. MATLAB®). The regularization tool [34] was used to determine the regularization parameter (λ). We used Intel (R) Core (TM) i7 CPU (2.90 GHz) laptop with 20 GB RAM for the simulation.
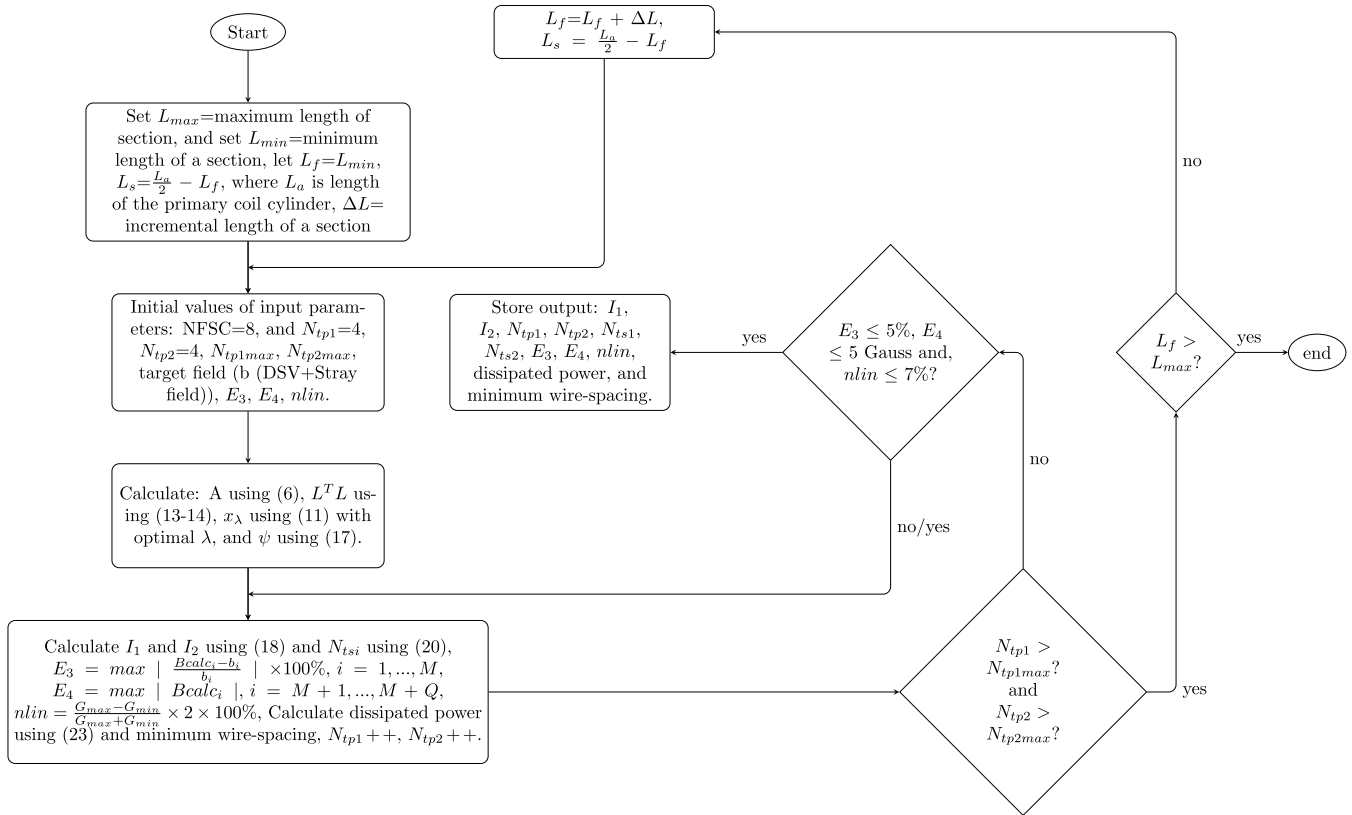
FIGURE 2. Flow chart diagram showing optimization of section dimension and number of turns. Here, *Bcalc* is the calculated magnetic field from the winding patterns, G_{max} and G_{min} are the maximum and the minimum calculated gradients, N_{tp1max} is the maximum number of turns of section one which was calculated from the length of the section by assuming a uniform coil distribution with wire spacing = 12 mm, *nlin* is the non-linearity (linearity error) of the calculated gradient on the DSV, E_3 is the maximum field deviation on the DSV, and E_4 is the maximum field strength on the stray field region. Note: the lengths of all shielding section coils are also proportionally updated simultaneously and the sign ' $=$ ' is the assignment operator.

TABLE 1. Dimensions of the two actively shielded Z-gradient cylindrical coils.

Item	First cylindrical coil		Second cylindrical coil	
	Radius (m)	Length (m)	Radius (m)	Length (m)
Primary coil	0.34	1.38	0.33	1.246
Shielding coil	0.40	1.48	0.38	1.286
Cryostat	0.45	1.60	0.43	1.46
DSV	0.50 m		0.50 m	
Gradient	30 mT/m		45 mT/m	

III. RESULTS

Similar to [4], the multi-channel and conventional Z-gradient coils were designed to produce a linear magnetic field gradient strength of $G_z = \partial B_z/\partial z = 30$ mT/m. The dimensions for the first and second conventional cylindrical coils are shown in TABLE 1. All results illustrated here are based on the first cylindrical coil dimensions. The second cylindrical coil dimensions are used to show that the power efficiency of the two-channel coil varies with the coil's dimension.

For the geometry optimization of the two-channel coils, different ratios of the surface divisions were considered. We started from $\frac{1}{10}$ of the total length of the cylinder (i.e., the first and fourth sections initially had a length of 13.8 cm, whereas the second and third sections had a length of 55.2 cm

each). Hence the total length of the cylinder is constant, as the length of the first section increases, the length of the second section decreases simultaneously (3). Accordingly, the size of the first section was increased with an incremental length ($\Delta L = 3.45$ cm) till it reaches 55.2 cm. The size of the second section was reduced proportionally till it reaches 13.8 cm at the same time as shown in Fig. 2. This resulted in a total of 13 different two-channel and 13 different three-channel coils. For the two-channel coils, the shielding sections were varied proportionally as those of the corresponding primary sections, whereas for all 13 coil designs of three-channel coils, the length of the shielding coil was fixed (similar to the conventional shielding coil). As a result, the optimal coil with low dissipated power keeping the maximum field deviation below 5% and stray field less than 5 Gauss (for 16×16 points distributed over the Z and θ directions at the cryostat) was found when the lengths of the first, second, third, and fourth sections for the primary surfaces of two-channel coils are 20.7 cm, 48.3 cm, 48.3 cm, and 20.7 cm, respectively. The corresponding sections of the two-channel shielding coil had lengths of 22.2 cm, 51.8 cm, 51.8 cm, and 22.2 cm, respectively. For the three-channel coils, out of the 13 possible designs, the coil with an optimal length of the primary 20.7 cm, 48.3 cm, 48.3 cm, and 20.7 cm for
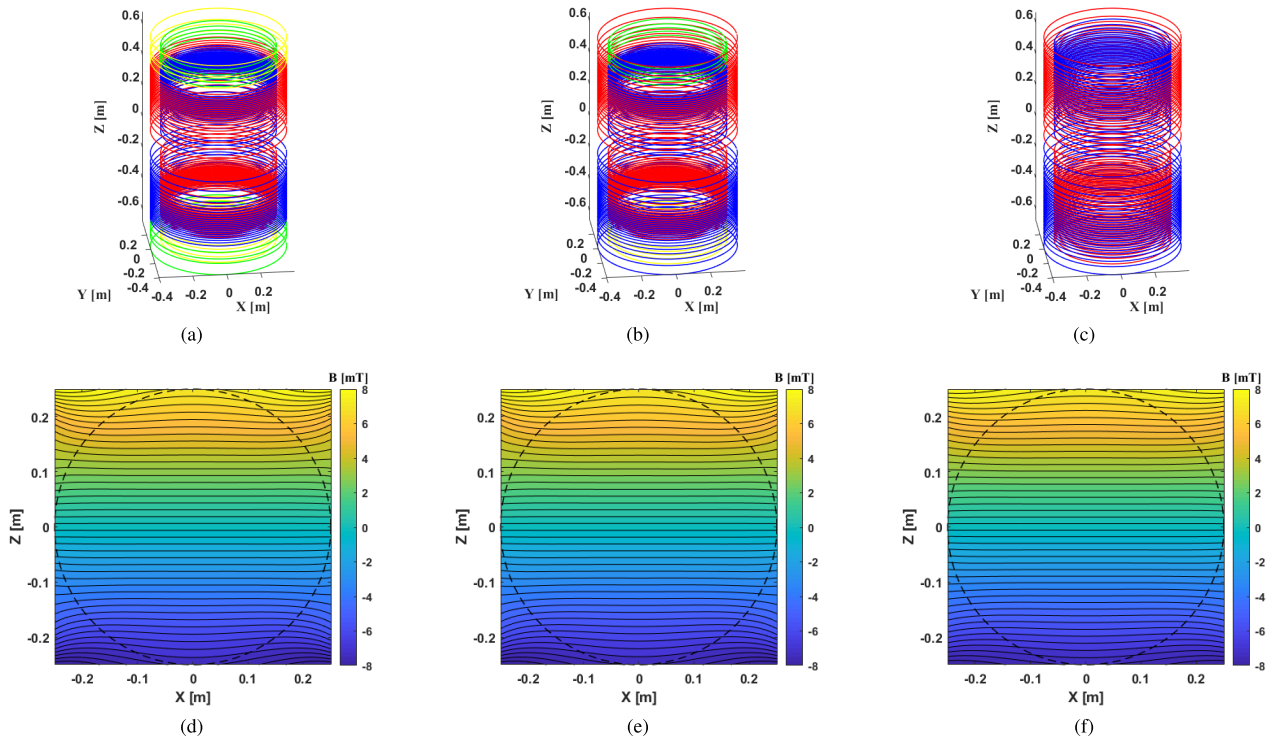
FIGURE 3. Designed multi-channel and conventional Z-gradient coils. 3D winding patterns for the power-efficient two-channel coil (a), three-channel coil (b), conventional coil (c); and their corresponding (d-f) field maps on the X-Z plane illustrating the gradient field. The dashed circle shows the desired operational region. In Fig. (a) and (b) green and blue windings have currents in the counter-clockwise direction, whereas yellow and red windings have currents in the clockwise direction.

sections one, two, three, and four, respectively had the best performances. For all three-channel coil configurations, the shielding coil had a length of 1.48 m.

The results of the most power-efficient coil out of 13 different designs from both two- and three-channel configurations are illustrated where they are compared to a designed conventional Z-gradient coil with similar dimensions.

Fig. 3 (a), (b), and (c) demonstrate the 3D winding patterns of two-channel, three-channel, and conventional Z-gradient coils, respectively. For the two-channel coils, the first channel consists of all yellow and green windings, whereas the second channel consists of all windings with blue and red colors. For the three-channel coils, the first and second channels on the primary coil surface have similar winding colors as those of the two-channel coil, whereas the third channel is the shielding coil with blue and red windings. For both coils, the sections with the same winding colors have currents in the same directions. For instance, for the primary two-channel Z-gradient coil, the first and second sections have currents in the counter-clockwise direction, whereas the third and fourth sections have currents in the clockwise direction. As shown in TABLE 2, the proposed two-channel coil requires less driving current per channel to generate the same gradient field on the DSV than the conventional coil. Similar to the two-channel configuration, the current of each channel of the three-channel coil was lower than that of the conventional coil as well.

To check the performance of the designed coils, the magnetic field maps on the X-Z plane were calculated from the winding patterns of Fig. 3 (a), Fig. 3 (b), and Fig. 3 (c) for two-channel, three-channel, and conventional coils, respectively using the Biot-Savart law and displayed at higher resolution as shown in Fig. 3 (d-f).

In our design, the calculated smallest distance between consecutive contours was 5.3 mm. So, when a copper wire with a track width of 4.0 mm is adopted as [4], the minimum wire gap will be 1.3 mm. The thickness and resistivity of copper wires were 5 mm and 1.68×10^{-8} Ωm, respectively [4]. The total resistance of each designed coil was then computed by using (22) which in turn was used to calculate the total dissipated power. Fig. 4 compares the total dissipated power of various configurations of two-channel, three-channel, and conventional coils with a fixed total number of turns on the primary coil cylinder (NT = 78). The dissipated DC power for the two-channel and three-channel coils are displayed by black and green curves, respectively, where the 13 stars stand for the dissipated power of 13 different coil configurations of both coils whose dimensions were calculated by using (3). The total dissipated powers of the most power-efficient two- and three-channel coils were less than that of the corresponding conventional coil by 25% and ~23%, respectively (see TABLE 2). As shown in TABLE 2, the multi-channel coils had also a better figure of power than the conventional coil.
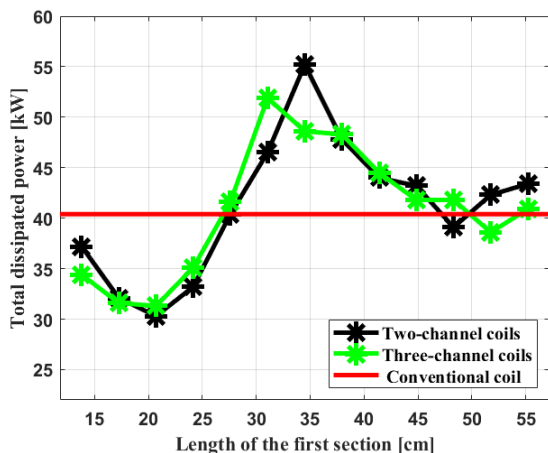
FIGURE 4. Total dissipated power comparison of 13 different configurations of two-channel, 13 different configurations of three-channel, and conventional coils. The black and green curves are used to determine the most power-efficient two-channel and three-channel coil configurations, respectively.
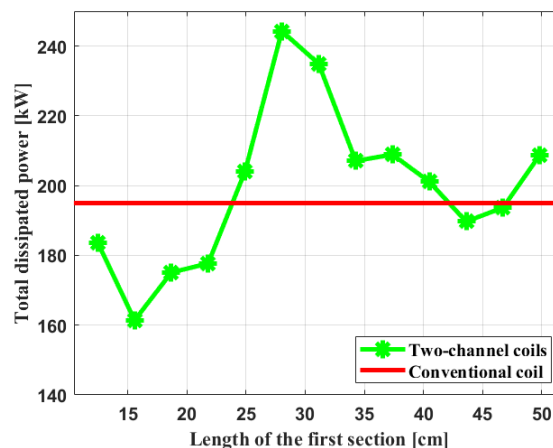

FIGURE 6. Total dissipated power comparison of 13 different configurations of two-channel and conventional coils using the second cylindrical coil dimensions shown in TABLE 1. The green curve is used to determine the most power-efficient two-channel coil configuration.
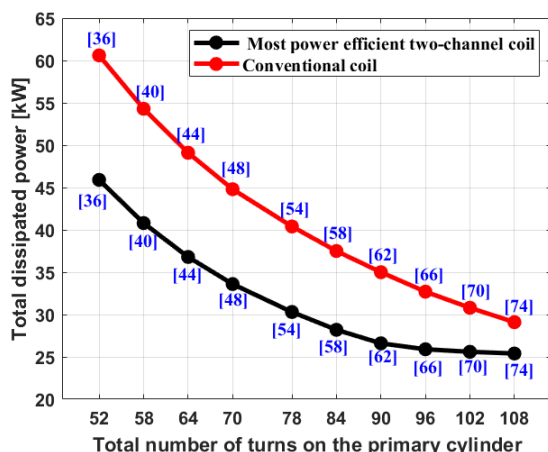

FIGURE 5. Total dissipated power comparison of the most power-efficient two-channel and conventional coil configurations as a function of the total number of turns on the primary coil surface. The number inside the square brackets on each dot represents the total number of turns for the corresponding shielding layer. The power efficiency of both two-channel and conventional coils increases as the total number of turns on the primary cylinder increases. The dissipated power reduction for the two-channel coil at a larger number of turns is comparably lower; however, a coil design with a large number of turns is not desirable as this increases the coil's inductance.

Fig. 5 shows the total dissipated power comparison of the most power-efficient two-channel coil with that of the conventional coil by varying the total number of turns on the primary cylinder from 54 to 108.

As shown in the figure, the two-channel coil has much lower dissipated power at a fewer number of turns compared to that of the conventional coil. As the number of turns increases, the two-channel coil still has a power dissipation advantage albeit with less efficiency. Increasing the number of primary turns for the single-channel coil, however, is not desirable as it increases the coil's inductance.

To understand better the power efficiency advantage for the two-channel design, different coil dimensions similar to [37] (the second cylindrical coil dimensions shown in TABLE 1) were used. The power reduction of the designed coils using these dimensions was comparably lower. First, the conventional and two-channel coils were designed by the proposed method with the same dimensions as [37]. Fig. 6 depicts the total power of 13 designs of two-channel coils and conventional coil. The power was reduced by 17% when the length of the first section is 15.58 cm. Here, the total powers of the designed coils are larger because the target gradient field was 45 mT/m and a 3 mm × 3 mm track cross-section was chosen. From the computed results, it has been observed that the longer the coil lengths, the higher the dissipated power reduction factor of multi-channel coils for the same number of turns on the primary coil cylinder.

Fig. 7 shows the comparison of maximum longitudinal stray magnetic flux densities at the cryostat for conventional, two-channel, and three-channel coils. As shown in the figure, multi-channel coils may have slightly better shielding efficiency as compared to the conventional coil.

Although we sampled the stray field along the Z direction similar to [4], we have noticed that the stray field is nearly constant along the θ direction and varies significantly along the Z direction. Accordingly, for better fidelity to achieve the desired shielding efficiency, we redesigned the coil configurations shown in Fig. 3 for target field points on the cryostat cylinder using 4×64 points in the θ and Z directions, respectively. The performances of all coils using the two target stray field sampling schemes (16×16 and 4×64) are tabulated in TABLE 2. The two-channel and three-channel coils still have a power dissipation reduction of ~28% and ~23%, respectively compared to the conventional coil. Fig. 8 (a-c) show the winding patterns of the redesigned power-efficient two-channel, three-channel, and conventional coils, respectively. Fig. 8 (d-f) show the magnitude of longitudinal stray
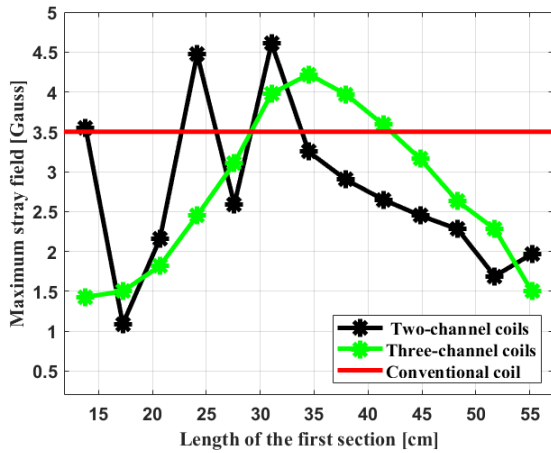
FIGURE 7. Comparison of maximum longitudinal stray magnetic flux densities for 13 different configurations of two-channel, 13 different configurations of three-channel, and conventional coils for 16 × 16 target stray field sampling scheme. The curves show that the most power-efficient two- and three-channel coils (configuration 3 for both cases) may have less maximum stray field strength compared to the conventional coil.

magnetic flux density maps for the redesigned two-channel, three-channel, and conventional coils, respectively, where the stray field pattern along the Z direction is illustrated. As shown in TABLE 2 and the maps in Fig. 8, the maximum stray field of each multi-channel coil is still slightly lower

than that of the conventional coil. The DC performances of the coils shown in Fig. 8 are tabulated in TABLE 2 where they have a target field performance in the operational region similar to Fig. 3 (d-f) (not illustrated to avoid redundancy).

IV. DISCUSSION

This study investigates the design of multi-channel Z-gradient coils by dividing the current-density surface into multiple sections along the length of the coil.

In a conventional, single-channel coil, the whole coil surface is driven by the same current, this, however, leads to a relatively large dissipated power in the coil. In our design, each channel is driven by an independent amplifier, and the total dissipated power of the proposed configuration is lower than that of the conventional coil.

In this study, the performances of 13 possible designs of two- and three-channel coils obtained by varying the length of each section while keeping the total number of turns on the primary cylinder equal were analyzed. A configuration with better performance was obtained when the second and first sections of the primary cylinder are 70% and 30% of the half-primary-coil length ($L_a/2$), respectively, for both two-channel and three-channel Z-gradient coils (Fig. 4).

Recently, Takrimi and Atalar [30] designed a 24-channel animal-size Z-gradient array coil with an active-shield array by dividing the primary and shielding coil surfaces into equal sections each. They aimed to achieve a dynamic DSV where

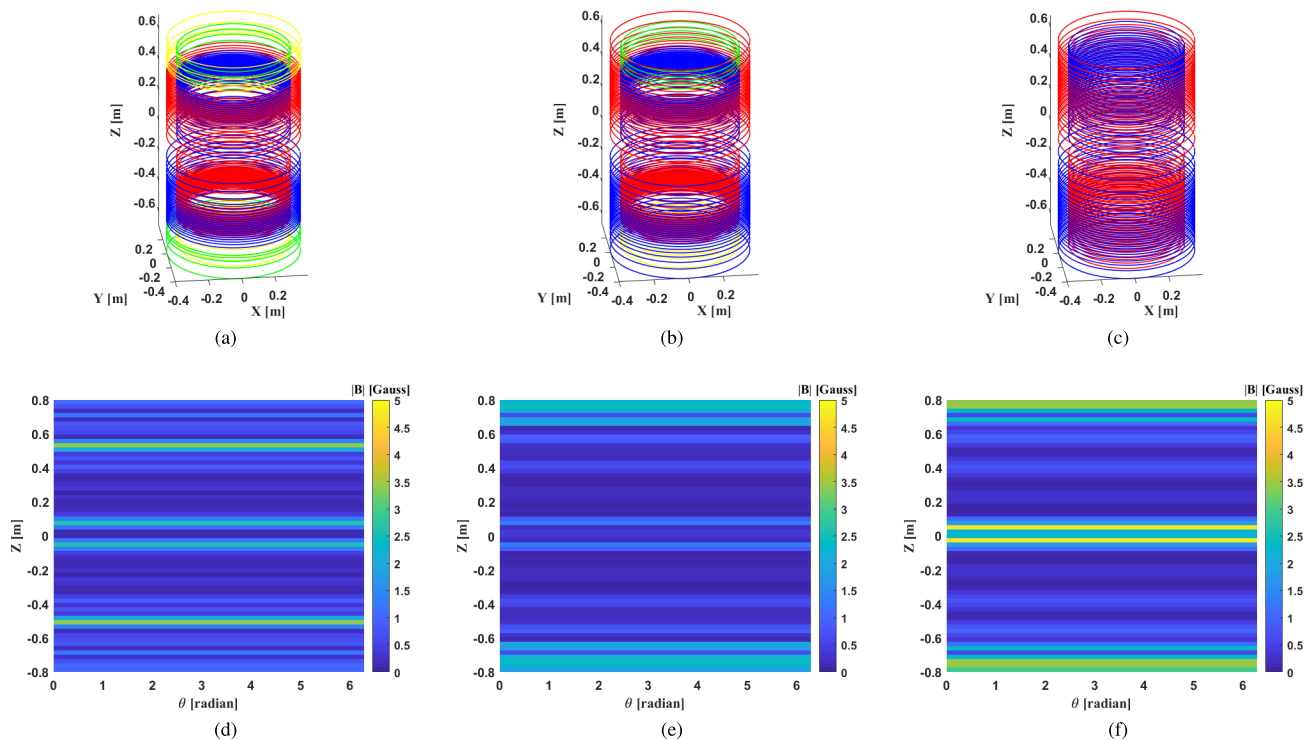**FIGURE 8.** Redesigned multi-channel and conventional Z-gradient coils for configurations illustrated in Fig. 3 using 4 × 64 points on the cryostat. 3D winding patterns for the power-efficient two-channel coil (a), three-channel coil (b), conventional coil (c); and their corresponding (d-f) stray field maps showing the magnitude of the longitudinal stray field component on the θ-Z plane (the display is for 16 × 64 points).

TABLE 2. Performance comparison of actively shielded two-channel, three-channel, and conventional Z-gradient coils.

Properties	Conventional coil		Two-channel coil			Three-channel coil		
	P	S	Channel	P	S	Channel	P	S (Ch.3)
Number of turns	78 (78*)	54 (54*)	Ch.1	10 (8*)	8 (10*)	Ch.1	10(10*)	54 (54*)
			Ch.2	68 (70*)	46 (46*)	Ch.2	68 (68*)	
Total resistance (mΩ)	254.00 (254.00*)		254.00 (258.20*)			254.00 (254.00*)		
Total power (kW)	40.40 (40.50*)		30.30 (28.80*)			31.30 (31.20*)		
Nonlinearity (%)	6.14 (6.16*)		6.69 (6.39*)			6.17 (6.22*)		
Maximum field deviation (%)	4.20 (3.90*)		4.07 (3.67*)			3.41 (3.44*)		
Maximum stray field (G)	3.56 (4.72*)		2.16 (3.37*)			1.82 (2.43*)		
Figure of power= $\frac{Gradient^2}{Total\ power}$ $(T^2 m^{-2} A^{-2} \Omega^{-1})$	2.25×10^{-8} (2.24×10^{-8}*)		2.95×10^{-8} (3.13×10^{-8}*)			2.91×10^{-8} (2.92×10^{-8}*)		
	P and S		Channel	P and S		Channel	P	S (Ch.3)
Current (A)	398.9 (399.5*)		Ch.1	294.2 (171.5*)		Ch.1	361.1 (351.3*)	349.1 (348.5*)
			Ch.2	352.7 (353.1*)		Ch.2	351.4 (352.0*)	
Wire width (mm)	4		4			4		
Wire thickness (mm)	5		5			5		
Minimum wire spacing (mm)	8.50 (8.80*)		5.60 (5.30*)			5.70 (5.70*)		

The variables Ch.1, Ch.2, and Ch.3 are channel one, channel two, and channel three, respectively. Similarly, P and S are primary and shielding, respectively. T =Tesla, G = Gauss, A = Ampere, kW =killo Watt, mΩ=milli Ohm, mm=milli meter. The performance metrics indicated by (*) are for the redesigned coils (Fig. 8 (a-c)) using the sampling scheme for the target stray field points of 4×64 along the θ and Z direction, respectively on the cryostat.

they placed their coil turns at equidistance fixed locations and optimized only the current per channel for each DSV location. For the conventional mode operation, Takrimi *et al.* achieved a 13% power reduction. In this work, we aim to design multi-channel coils just operating in a conventional mode using a minimal number of channels where we optimize for the coil distribution patterns, driving currents, and section size. The DC characteristics for our multi-channel coil designs compare well to the conventional single-channel coil. We have noticed that the stray field is nearly constant along the θ direction and varies significantly along the Z direction as shown in Fig. 8 (d-f). Also, when computing the high resolution stray field maps for the coils designed using the 16 × 16 sampling scheme for the target stray field, the maximum stray field noticeably increased. Accordingly, for better fidelity to achieve the desired shielding efficiency, we redesigned the power-efficient two-channel, three-channel, and conventional coil configurations using a 4×64 sampling scheme (keeping $Q = 256$ for computational efficiency). We observed that the achieved maximum stray fields for the redesigned coils do not noticeably change for higher resolution maps. As a result, we recommend the configurations reported in Fig. 8. Generally, we achieved 17-28% and ∼23% power reduction using the two- and three-channel coils, respectively. The findings of the study suggest that coils with less operating DC power requirements can be designed by dividing conventional coils into more than one channel. Similar to the findings of the two-channel whole-body RF coil [38], it was observed that the two-channel gradient coil can operate with less dissipated DC power compared to the single-channel configuration. It is also shown that the power reduction factor is dependent on the gradient coil's geometrical dimensions and number of turns (Fig. 4-6) as well as the design parameters.

High-performance gradient coils are usually needed to provide high maximum gradient field strength for high spatial resolution MRI used in neuroimaging applications [39],

[40]. Also, diffusion-weighted imaging and diffusion tensor imaging (DTI) which are important imaging modalities for diagnosing neurological disorders and mapping brain connectivity require high-performance gradients [41], [42], [43]. The findings of this study may thus be applied to the design of high gradient field MRI applications as indicated where power considerations become critical.

V. CONCLUSION

In this work, a new methodology for designing two- and three-channel Z-gradient coils is presented. The performances of the designed multi-channel coils are compared to those of a single-channel conventional coil with similar dimensions and DC performance metrics. The following points are specifically attained:

- Using Fourier series expansion approximation of current densities, a framework was developed to optimize multi-channel Z-gradient coil design.
- The distribution of the windings, current per channel, and sectional size were optimized to achieve the least possible dissipated power for the multi-channel coil design performing with the desired DC characteristics.
- Power efficiency gains for two- and three-channel, whole body, Z-gradient coils of 17-28% and ∼23% were achieved, respectively.
- It was also shown that the power efficiency depends on the coil's dimension, number of turns, and design parameters.
- The importance of the sampling scheme used for the target stray field during the design process, while not changing the total number of points for computational efficiency, is noted.

The findings of this study may thus be applied to the design of high gradient field MRI applications where gradient coils yielding high gradient fields are needed and their operating power requirements become critical. Currently, the more challenging problem of determining the power reduction gain

of multi-channel transverse gradient coil designs is further investigated using the discrete wire design method [44]. In the future, practical implementations for such multi-channel gradient configurations may be performed where channel coupling considerations among other aspects are to be studied.

REFERENCES

[1] R. Turner, "Gradient coil design: A review of methods," *Magn. Reson. Imag.*, vol. 11, no. 7, pp. 903–920, 1993.

[2] S. S. Alsharafi, A. M. Badawi, and A.-M.-M. El-Sharkawy, "Design of a self-shielded transverse MRI gradient coil taking into account track width," in *Proc. IEEE 5th Middle East Afr. Conf. Biomed. Eng. (MECBME)*, Oct. 2020, pp. 1–4.

[3] R. Turner, "A target field approach to optimal coil design," *J. Phys. D, Appl. Phys.*, vol. 19, no. 8, pp. 147–151, Aug. 1986.

[4] M. Zhu, L. Xia, F. Liu, J. Zhu, L. Kang, and S. Crozier, "A finite difference method for the design of gradient coils in MRI—An initial framework," *IEEE Trans. Biomed. Eng.*, vol. 59, no. 9, pp. 2412–2421, Sep. 2012.

[5] F. Jia, Z. Liu, M. Zaitsev, J. Hennig, and J. G. Korvink, "Design multiple-layer gradient coils using least-squares finite element method," *Struct. Multidisciplinary Optim.*, vol. 49, no. 3, pp. 523–535, Sep. 2013.

[6] F. Tang, J. Hao, F. Freschi, C. Niu, M. Repetto, F. Liu, and S. Crozier, "A cone-shaped gradient coil design for high-resolution MRI head imaging," *Phys. Med. Biol.*, vol. 64, no. 8, Apr. 2019, Art. no. 085003.

[7] F. Tang, "Gradient coil design and intra-coil eddy currents in MRI systems," Ph.D. dissertation, School Inf. Technol. Elect. Eng., Univ. Queensland, Brisbane, QLD, Australia, 2016.

[8] L. Marin, H. Power, R. W. Bowtell, C. C. Sanchez, A. A. Becker, P. Glover, and A. Jones, "Boundary element method for an inverse problem in magnetic resonance imaging gradient coils," *Comput. Model. Eng. Sci.*, vol. 23, no. 3, pp. 149–173, 2008.

[9] C. C. Sanchez, S. G. Garcia, L. D. Angulo, C. M. D. J. Van Coevorden, and A. R. Bretones, "Divergence free BEM to model quasi-static currents, application to MRI coil design," *Prog. Electromagn. Res. B*, vol. 20, pp. 187–203, 2010.

[10] G. N. Peeren, "Stream function approach for determining optimal surface currents," *J. Comput. Phys.*, vol. 191, no. 1, pp. 305–321, Oct. 2003.

[11] M. A. Brideson, L. K. Forbes, and S. Crozier, "Determining complicated winding patterns for shim coils using stream functions and the target-field method," *Concepts Magn. Reson.*, vol. 14, no. 1, pp. 9–18, 2002.

[12] S. Zheng, X. Li, W. Qi Yan, and W. Xu, "Gradient coils design with regularization method for superconducting magnetic resonance imaging," in *Proc. Int. Conf. Image Vis. Comput. (IVCNZ)*, Nov. 2018, pp. 1–5, doi: 10.1109/ivcnz.2018.8634786.

[13] T. N. Baig, T. P. Eagan, L. S. Petropoulos, T. K. Kidane, W. A. Edelstein, and R. W. Brown, "Gradient coil with active endcap shielding," *Concepts Magn. Reson. B, Magn. Reson. Eng.*, vol. 31B, no. 1, pp. 12–23, 2007.

[14] L. S. Petropoulos and S. J. Ling, "Flared gradient coil set with a finite shield current," U.S. U.S. Patent 6 078 177-A, Jun. 20, 2000.

[15] R. Zhang, J. Xu, Y. Fu, Y. Li, K. Huang, J. Zhang, and J. Fang, "An ptimized target-field method for MRI transverse biplanar gradient coil design," *Meas. Sci. Technol.*, vol. 22, no. 12, Dec. 2011, Art. no. 125505.

[16] W. Liu, D. Zu, X. Tang, and H. Guo, "Target-field method for MRI biplanar gradient coil design," *J. Phys. D, Appl. Phys.*, vol. 40, no. 15, pp. 4418–4424, 2007.

[17] T. Morrone, "Optimized gradient coils and shim coils for magnetic resonance scanning system," U.S. Patent 5 760 582-A, Jun. 2, 1998.

[18] J. Wang, B. Zhou, X. Liu, W. Wu, L. Chen, B. Han, and J. Fang, "An improved target-field method for the design of uniform magnetic field coils in miniature atomic sensors," *IEEE Access*, vol. 7, pp. 74800–74810, 2019.

[19] P. T. While, L. K. Forbes, and S. Crozier, "An inverse method for designing RF phased array coils in MRI-theoretical considerations," *Meas. Sci. Technol.*, vol. 18, no. 1, pp. 245–259, 2007.

[20] S. Wintzheimer, F. Fidler, M. Ledwig, T. Drieble, D. Gensler, and P. M. Jakob, "Novel gradient design: Simultaneous generation of fast switchable linear and high order field gradient for MR imaging," in *Proc. ISMRM*, 2009, p. 3059.

[21] S. Wintzheimer, T. Driessle, M. Ledwig, P. M. Jakob, and F. Fidler, "A 50-channel matrix gradient system: A feasibility study," in *Proc. ISMRM*, vol. 18, 2010, p. 3937.

[22] S. Littin, F. Jia, K. J. Layton, S. Kroboth, H. Yu, J. Hennig, and M. Zaitsev, "Development and implementation of an 84-channel matrix gradient coil," *Magn. Reson. Med.*, vol. 79, no. 2, pp. 1181–1191, Feb. 2018.

[23] C. Juchem, T. W. Nixon, S. McIntyre, D. L. Rothman, and R. A. D. Graaf, "Magnetic field modeling with a set of individual localized coils," *J. Magn. Reson.*, vol. 204, no. 2, pp. 281–289, Jun. 2010.

[24] K. Setsompop, R. Kimmlingen, E. Eberlein, T. Witzel, J. Cohen-Adad, J. A. McNab, B. Keil, M. D. Tisdall, P. Hoecht, P. Dietz, and S. F. Cauley, "Pushing the limits of *in vivo* diffusion MRI for the human connectome project," *NeuroImage*, vol. 80, pp. 220–233, Oct. 2013.

[25] F. Jia, G. Schultz, F. Testud, A. M. Welz, H. Weber, S. Littin, H. Yu, J. Hennig, and M. Zaitsev, "Performance evaluation of matrix gradient coils," *Magn. Reson. Mater. Phys., Biol. Med.*, vol. 29, no. 1, pp. 59–73, Feb. 2016.

[26] F. Jia, S. Littin, K. J. Layton, S. Kroboth, H. Yu, and M. Zaitsev, "Design of a shielded coil element of a matrix gradient coil," *J. Magn. Reson.*, vol. 281, pp. 217–228, Aug. 2017.

[27] K. Ertan, S. Taraghinia, A. Sadeghi, and E. Atalar, "A Z-gradient array for simultaneous multi-slice excitation with a single-band RF pulse," *Magn. Reson. Med.*, vol. 80, no. 1, pp. 400–412, Jul. 2018.

[28] S. Taraghinia, "A Z gradient coil array system for magnetic resonance imaging," M.S. thesis, Dept. Elect. Electron. Eng., Bilkent Univ., Ankara, Turkey, Jan. 2016.

[29] M. Takrimi and E. Atalar, "A programmable set of Z gradient array and active shield array for magnetic resonance imaging," in *Proc. 28th Annu. Meeting (ISMRM)*, 2020, p. 4242.

[30] M. Takrimi and E. Atalar, "A z-gradient array coil with a dedicated active-shielded array coil for MRI," *Magn. Reson. Med.*, pp. 1–14, Aug. 2022, doi: 10.1002/MRM.29390.

[31] H. B. Kassahun, S. S. Alsharafi, A. M. Badawi, and A. M. El-Sharkawy, "Towards a more power-efficient two-channel biplanar Z-gradient coil design using target field method," in *Proc. ISMRM*, Apr. 2021, p. 3097.

[32] P. C. Hansen, "REGULARIZATION TOOLS: A MATLAB package for analysis and solution of discrete ILL-posed problems," *Numer. Algorithms*, vol. 6, pp. 1–35, Mar. 1998.

[33] J. Müller and S. Siltanen, *Linear and Non-Linear Inverse Problems With Practical Applications*, Philadelphia, PA, USA: Society for Industrial and Applied Mathematics, 2012.

[34] P. C. Hansen. (2001). *Regularization Tools: A MATLAB Package for Analysis and Solution of Discrete ILL-Posed Problem*. [Online]. Available: http://www.imm.dtu.dk/pch

[35] L. K. Forbes and S. Crozier, "A novel target-field method for magnetic resonance shim coils: III. Shielded zonal and tesseral coils," *J. Phys. D, Appl. Phys.*, vol. 36, no. 2, pp. 68–80, 2003.

[36] X. Ping, H. Wang, Q. Li, X. Yin, X. Wang, and C. Li, "A discussion on the solution of linear systems appeared in gradient coil optimization with the finite element method," *Appl. Magn. Reson.*, vol. 51, no. 4, pp. 363–373, Apr. 2020.

[37] Y. Wang, X. Xin, F. Liu, and S. Crozier, "Spiral gradient coil design for use in cylindrical MRI systems," *IEEE Trans. Biomed. Eng.*, vol. 65, no. 4, pp. 911–920, Apr. 2018.

[38] J. Nistler, D. Diehl, W. Renz, and L. Eberler, "Homogeneity improvement using a 2 port birdcage coil," in *Proc. ISMRM*, 2007, p. 1063.

[39] S. A. Winkler, F. Schmitt, H. Landes, T. Wade, A. Aljeski, and B. K. Rutt, "Gradient and shim technologies for ultra high field MRI," *Neuroimage*, vol. 168, pp. 59–70, Mar. 2018.

[40] B. Vachha and S. Y. Huang, "MRI with ultrahigh field strength and high-performance gradients: Challenges and opportunities for clinical neuroimaging at 7 T and beyond," *Eur. Radiol. Experim.*, vol. 5, no. 1, pp. 1–18, Dec. 2021.

[41] P. Mukherjee, J. I. Berman, S. W. Chung, C. P. Hess, and R. G. Henry, "Diffusion tensor MR imaging and fiber tractography: Theoretic underpinnings," *Amer. J. Neuroradiology*, vol. 29, no. 4, pp. 632–641, Apr. 2008.

[42] P. Mukherjee, S. W. Chung, J. I. Berman, C. P. Hess, and R. G. Henry, "Diffusion tensor MR imaging and fiber tractography: Technical considerations," *Amer. J. Neuroradiology*, vol. 29, no. 5, pp. 843–852, May 2008.

[43] T. K. F. Foo, E. T. Tan, and M. E. Vermilea, "Highly efficient head-only magnetic field insert gradient coil for achieving simultaneous high gradient amplitude and slew rate at 3.0T (MAGNUS) for brain microstructure imaging," *Magn. Reson. Med.*, vol. 83, no. 6, pp. 2356–2369, Jun. 2020.

[44] H. B. Kassahun, S. S. Alsharafi, A. M. Badawi, and A. M. El-Sharkawy, "Actively shielded two-channel transverse MRI gradient coil numerical design using discrete wire method," in *Proc. Joint Annu. Meeting ISMRM-ESMRMB ISMRT 31st Annu. Meeting Hybrid Exper.*, London, U.K., 2022, p. 3250.

HAILE BAYE KASSAHUN received the B.Sc. degree in electrical and computer engineering and the M.Sc. degree in biomedical engineering from Addis Ababa University, in 2013 and 2017, respectively. He is currently pursuing the Ph.D. degree with the Department of Systems and Biomedical Engineering, Cairo University. He worked as an Assistant Lecturer with the Center of Biomedical Engineering, Addis Ababa University, from 2014 to 2017. His research interests include MRI gradient coil design, medical physics, medical imaging, and biomedical image processing.

SADEQ S ALSHARAFI (Member, IEEE) received the B.Sc. and M.Sc. degrees from the Systems and Biomedical Engineering Department, Faculty of Engineering, Cairo University, in 2006 and 2011, respectively, where he is currently pursuing the Ph.D. degree with the Department of Systems and Biomedical Engineering. He is also a Lecturer at the Biomedical Technology Department, Sana'a Community College, Yemen. He has published around nine journals and conference publications and a book. His research interests include MRI gradient coil design, biomedical image processing, biomedical optics, and biomedical instrumentation.

AHMED M BADAWI (Senior Member, IEEE) received the B.Sc., M.Sc., and Ph.D. degrees from the Systems & Biomedical Engineering (SBME) Department, Cairo University, Egypt, in 1990, 1993, and 1996, respectively. He was promoted to an Assistant Professor, an Associate Professor, and a Full Professor, in 1996, 2001, and 2007, respectively. He was the SBME Department Chairman, from 2013 to 2019. He is currently a Full Professor at the SBME Department. He worked as a Visiting Professor at the Biomedical Engineering Department, The University of Tennessee Knoxville, USA, from 2005 to 2007, and a Senior Research Fellow at the Medical Physics Department, Virginia Common Wealth University, VA, USA. He was the Program Chair and the General Chair of the Cairo International Biomedical Engineering Conference (CIBEC08 and CIBEC14). He chaired tens of session at IEEE conferences starting IEEE 2003 Midwest Conference in Circuits and Systems. He reviewed several papers with IEEE, IEEE/EMBC, and others. He received several awards, Egyptian State Award for research, in 2001, and Cairo University Research Award, in 2002. He has got 30 years of experience in academia and industry in the areas of multidimensional image analysis, pattern recognition, computer vision, and AI in medicine. He has participated and lead the team who put a strategy and roadmap for digitally transforming health sector in Egypt (eHealth and comprehensive health insurance) via a grant from National Telecommunication Regulation Authority (NTRA). He is also the Leader of Cairo University African Biomedical Engineering Mobility (ABEM) Program funded from European Union to six African Universities.

ABDEL-MONEM M EL-SHARKAWY (Member, IEEE) received the B.Sc. and M.Sc. degrees in systems and biomedical engineering (SBME) from Cairo University, Cairo, Egypt, and the M.Sc. and Ph.D. degrees in electrical and computer engineering from Johns Hopkins University (JHU), Baltimore, MD, USA, in 2004 and 2008, respectively. He worked as a Research Faculty Instructor at the Radiology Department, JHU, from 2008 to 2014. He is currently an Associate Professor at SBME, Cairo University, and the Chairman of the National Academy of Information Technology for Person with Disabilities (NAID) at the Egyptian Ministry of Communications and Information Technology (MCIT). From 1998 to 2001, his research work was focused on ultrasound medical imaging related topics. He has been involved with magnetic resonance imaging (MRI) research, since 2002. His research interests include medical imaging, medical physics, computations and instrumentation, and eHealth, digital transformation, and assistive technologies. His article on high field signal-to noise-ratio performance of the MR loopless antennas was featured as the cover picture for the May 2008 issue of the *Medical Physics* journal. He currently has about 23 peer reviewed journal articles, three U.S. published patents, and more than 60 conference presentations. His current H-index is 15.

• • •